Smart Materials and Structures

TECHNICAL NOTE • **OPEN ACCESS**

A new concept of structural smart fabric activated by shape memory alloys

To cite this article: Luca Mariotti *et al* 2024 *Smart Mater. Struct.* **33** 127001

OPEN ACCESS
IOP Publishing
Smart Materials and Structures
Smart Mater. Struct. **33** (2024) 127001 (11pp)
https://doi.org/10.1088/1361-665X/ad8d26

Technical Note

A new concept of structural smart fabric activated by shape memory alloys

Luca Mariotti, L Patriarca, Marco Rossoni, Paolo Parenti and Luca Michele Martulli*

Politecnico di Milano, Mechanical Engineering Department, Via La Masa 1, 20156 Milano, Italy

E-mail: lucamichele.martulli@polimi.it

Received 24 July 2024, revised 18 October 2024
Accepted for publication 30 October 2024
Published 12 November 2024

Abstract

This work presents the development, prototyping and validation of a new concept of structure called structural smart fabric (SSF). An SSF is a chainmail fabric composed by interconnected elements, called cells, which can be stiffened by reactive elements, such as those made by shape memory alloy (SMA). Exploiting the shape memory functionality, SSFs are capable of sensing and reacting to external stimuli. Based on this concept, in this study we propose an SSF that integrates SMA wires into a 3D-printed chainmail structure. The shape memory effect of these wires is used as an actuating mechanism that, at high temperature, tightens the adjacent cells together and provides increased structural stiffness. In this study, finite element simulations were initially conducted to enhance the comprehension of the SSF's mechanical behaviour. The influence of the initial cell spacing on the SSF stiffness and the wire stress profiles was evaluated during bending loading, as well as the evolution of contact pressure profiles between adjacent cells. This numerical approach enabled to tune the design of the SSF prototypes which were successively manufactured using selective laser sintering additive manufacturing technology with PA12. After the integration with the SMA wires, the SSF prototypes were tested under a 3-point bending configuration at different temperatures. The results revealed a remarkable increase in structural stiffness at elevated temperatures compared to ambient conditions. This study set the basis for a deeper understanding of SSF's unique capabilities and potential applications in fields where adaptive and responsive structures are required.

Keywords: smart structures, fabrics, variable stiffness, 3D printing, chainmail, SMA

1. Introduction

In recent years, the widespread use of 3D printing allowed the global research to explore new concepts for meta-materials and structures [1–3]. Among these, structures inspired by the chainmail armours of the Middle Ages were investigated [4]. These structures are composed by interconnected elements, called cells, which maintain partial freedom of relative motion. This allows the chainmail to behave like a fabric. Some applications of chainmail fabrics range from fashion [4–7] to biomedical [8–10] and robotic engineering [11]. According to the requirements of the specific application, chainmail fabrics can reach different sets of mechanical characteristics by exploiting the intrinsic material properties and the geometry of the cells [10, 12]. In this regard, 3D printing allows high geometrical flexibility for the cells and a one-step manufacturing of large fabrics, thus drastically reducing assembling times and costs [11, 13]. Smart materials, i.e. materials with adaptive features and functions capable of reacting to external stimuli, are also

* Author to whom any correspondence should be addressed.

a product of the recent technological development [14, 15]. In this context, chainmail fabrics can be further improved into smart fabrics, as shown in the literature by a few pioneering works [8, 10, 11, 16].

Ploszajski *et al* [8] developed a 4D printed chainmail with double stiffness for a wearable assistive device such as orthotics. This was a nylon chainmail composed of hollow cubes, which was immersed in a ferrofluid bath and then dried. This treatment covered the polymer particles with a dry ferrofluid micro-layer and the polymeric structure became sensitive to an applied magnetic field. Upon contact with a magnetic surface, the fabric exhibited increased stiffness due to the jamming of the cubes. The increase in stiffness was only qualitatively evaluated from the fabric shape, without an actual quantitative measure. The authors suggested a potential use in the biomedical sector as an actively stiffened wrist-brace. However, the proposed solution required the creation of a sufficiently powerful magnetic field directly in the exoskeletal device. Such a device would thus not be easily portable and would require an additional source of energy to operate the electromagnet [8]. The authors also investigated other activation inputs such as swellable hydrogels, granular media, electroactive polymers and pneumatic systems. However, these proved non-ideal in terms of performance, or not feasible.

Another prototype of chainmail smart fabric with variable stiffness manufactured by 3D printing was developed by Wang *et al* [10]. Under inactive conditions, the chainmail showed near-zero bending stiffness, thus behaving like a fabric. However, when placed in a sealed envelope under vacuum, the fabric became stiff with load bearing capabilities. Several cell designs were evaluated, all made by connected trusses to allow relative interconnection. Bending and impact tests were performed to characterise the stiffened fabric. The maximum stiffness increase obtained was tenfold compared to the loose configuration. Interestingly, the stiffness could be adjusted to a desired value by changing the suction pressure. The tuneable stiffness, rather than a simple active or inactive state, widens the application landscape. However, the suction pressure requires the availability of a vacuum pump; this can be a limit to the portability and energy efficiency of the fabric.

In the fore-mentioned works, smart fabrics were obtained using additional external devices (vacuum pump, electromagnet), which increase the undesired weight, volume, energy consumption and potentially lower the reliability of the whole system. The use of smart materials with intrinsic sensing and/or actuation properties can potentially solve this issue [5, 15]. These materials are capable of responding to the environment, or external stimuli, of different nature that modify their physical properties [17]. Smart materials can thus be combined with structural fabrics to make them reactive to a certain environmental stimulus [10].

Shape memory alloys (SMAs) represent an example of metallic materials capable of producing an actuation force induced by an external stimulus thanks to a reversible austenitic-martensitic phase transformation. The most successful SMA is nitinol (commercial names derived from composition and place of discovery: Nickel Titanium-Naval Ordnance Laboratory) where nickel and titanium are combined in equal atomistic concentration [18]. The original shape of a SMA component can be restored, after a large plastic deformation, by simply heating up the material. This is caused by a microstructural transition from the low temperature phase (martensite) to the high temperature phase (austenite) [18, 19]. This property can be exploited to actuate a mechanical system, SMAs are indeed used in several robotic applications [20, 21], also thanks to their high energy density [18, 19, 22]. It should be noted that a precursor of the prototype presented in this study was proposed by Yuen *et al* [16] which involves the sewing of straightened SMA helical coils on a woven fabric with the aim to create motion on the fabric. When heated via Joule effect, the coils recovered their helical shape generating a pulling force on the fabric to compress it or bend it with actuating force in the order of 1–10 N [16]. SMA coils were also used by Ransley *et al* [11] in the activation of a 3D printed chain for soft robotic applications (only a single row of cells was studied). The chain was constituted of interlinked hollow square elements. These were 3D printed in two half squares that were later assembled and integrated with the SMA coils. The two half squares can slide one inside the other changing the length of two parallel edges of the square. The sliding was driven by the SMA actuators heated through the Joule effect, and it caused all the elements to jam one on each other. The prototype had two primary states, open and closed, with the maximum stiffness in its closed configuration. For this prototype [11], the chain could be bent only in one direction, due to the asymmetrical cells shape. Furthermore, a one-shot manufacturing was not possible, and the assembly phase remained quite complex.

Both the works of Yuen *et al* [16] and Ransley *et al* [11] considered an actuation based on SMA wires transforming from straight lines to spiral coils. This allows to achieve a large longitudinal displacement, while actuation forces are generally small, and this limits the achievable stiffness.

The present work proposes an innovative 3D printed structural smart fabric (SSF) with temperature-dependent stiffness. This characteristic can be exploited in many field: from biomedical application such as wearable exoskeletons to the space environment [23, 24]. In particular, regarding space applications the proposed SSF is especially suitable for deployable structure that can gain stiffness the desired stiffness once in place. The SSF is composed by interconnected cells featuring SMA wires. The SMA wires were inserted inside holes in the cells and they were kept in a straight shape (rather than coil shape), as this shape generates the highest level of force with respect to the amount of used material [18]. The fabric composed only by the interconnected cells will be referred to as *chainmail* in the rest of the work, while, after the integration with the SMA wires, it will be referred to as *SSF*.

Below the SMA transformation temperature (70 °C for the SMA used in this work [25]), the fabric displays low bending stiffness. The initial clearance between the cells granted the SSF to behave as a fabric (i.e., with a low to near-zero bending stiffness) at low temperature. This configuration will be called *inactive* in the rest of the work. Above this temperature, the wires shrink, jamming the cells together and thus increasing the rigidity of the whole fabric. The contraction of the wires is

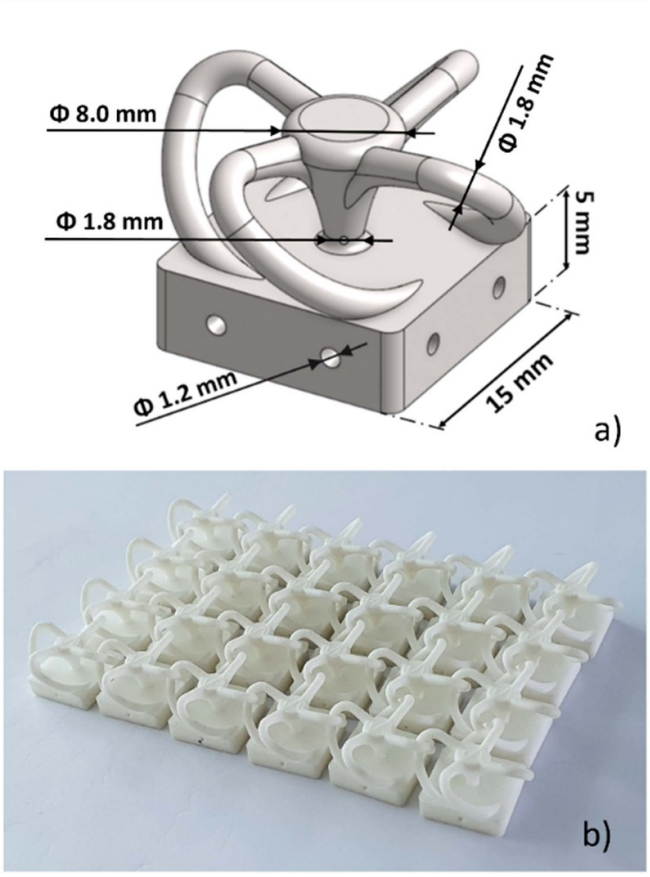

Figure 1. (a) Single cell model with characteristic dimensions; (b) example of a 6 × 4 cells chainmail.

indeed prevented by the presence of the cells. This configuration will be called *active* in the rest of the work.

2. Materials and methods

2.1. Design, manufacturing and assembling of the SSFs

The cells are composed of a flat squared plate on one side and a system of branches on the other side, as shown in figure 1(a). Their design of the proposed fabric's cells was inspired and adapted by the one proposed by NASA [26]. The plate hosts the wires and, in the active configuration, is the load-bearing structural element of the cell. The branches allow mutual interconnections among all the cells of the chainmail and maintain them in position during the integration of the wires.

Compared to the original NASA design [26], the system of connecting branches was simplified as much as possible to have a light structure and to reduce the mutual interference of the cells, by enhancing the range of motion in unloaded conditions. The considered cell design and dimensions of the prototypes tested in this work are shown in figure 1(a). The dimensions of the plate were chosen as a compromise between the load bearing capabilities of the SSF in the active configuration, the manufacturing requirements, and the necessity to host the SMA wires into the cells. Nevertheless, other dimensions and designs are also possible for different requirements. The chainmail was designed to be additively manufactured in a single component, thus with the cells already interconnected.

Table 1. PA12 material properties by the supplier (EOS).

Tensile modulus	1650 (MPa)
Tensile strength	48 (MPa)
Nominal strain at break	18 (%)
Melting temperature (20 °C min^{-1})	176 (°C)
Density	930 (kg m^{-3})

All the chainmail specimens produced in this work were made of PA12 nylon (the powder was the PA 2200 supplied by EOS with properties reported in table 1 [27]) and they were manufactured using selective laser sintering technology on an EOS Formiga P110 Velocis printer. The choice of a polymeric material for the cells was made considering the low production cost and time. Nevertheless, the working principle of the proposed SSF can also be implemented with alternative chainmail materials. In figure 1(b) a picture of a 6 × 4 cells fabric was reported to have a clear view on the chainmail interconnection among adjacent cells.

Regarding the tested SSF prototypes, they featured 15 cells in a 5 × 3 configuration, as shown in figure 2. Two parallel SMA wires were inserted in each plate, which allowed higher bending forces to be applied in the experimental campaign. The chosen SMA wires were the NiTi/54/W/0.5/T of SAES Getters Spa manufacturer [25], with a diameter of 0.5 mm. These were applied only along one direction of the SSF and each wire was fixed at the two ends of the chainmail with wire clamps. The wires were previously two-way trained by the manufacturer to shorten at high temperature. As the maximum recoverable strain of the SMA at high temperature is fixed, the initial space between the plates upon assembling with the SMA wires influences the contact pressure between the plates created by the system activation. The tested prototypes were all assembled with a target initial plate spacing of 1 mm which was selected from FE simulations as discussed in the following. Brass laminas with calibrated thicknesses of 1 mm were inserted between the plates during the assembling phase. Therefore, the wires length resulted to be 50 mm that corresponds to the length of three in line plates plus 1 mm for each spacing among the plates; the total length resulted in 52 mm.

Four specimens nominally identical were manufactured and tested (same geometry, same manufacturing technique, same theoretical plates spacing).

Note that, to ensure easier testing under the 3-point bending configuration, some branches of the external plates were removed, while the cells on one of the sides featured a housing for the rollers of the testing equipment (highlighted in figure 2 and described in section 2.2). These operations are specific for the tests of this work and are not required for the full operation of the SSF as the prototype already shown in figure 1(b). Moreover, this highlights the versatility of the proposed SSF, that can feature branches and plates of different shapes, or even a reduced number of branches.

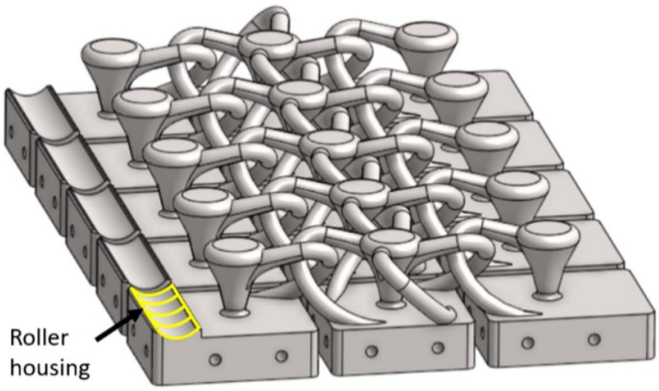

Figure 2. 3D model of the specimen with the roller housing highlighted.

2.2. Experimental characterisation and validation

The experimental work consisted in two main phases. First, the material mechanical properties of the SMA wires and of the PA12 were characterised at room and high temperature. These material properties were used in the finite element (FE) simulations of the entire SSFs. Then, three-point bending tests were performed on the four SSF prototypes to validate their tuneable stiffness with temperature variations.

All the tests were performed using an MTS Alliance RF/150 testing machine equipped with a load cell of 150 kN. Three temperatures were chosen as reference in the entire experimental campaign: 80 °C, 90 °C and 100 °C. These were all chosen above the SMA transformation temperature of about 70 °C in stress-free condition declared in the manufacturer datasheet [25]. Moreover, the 10 °C interval ensures a significant variation in the transformation stresses of the super-elastic cycle. This was evaluated using the transformation temperature diagram in the manufacturer datasheet [25]. All high temperature tests were performed using an MTS 651 environmental chamber mounted on the testing machine as shown in figure 3(a).

2.2.1. SMA wires tests. Wire specimens were cut with a length of 100 mm and tested inside the environmental chamber. This wire length was chosen to better fit with the testing equipment of the employed machine. The same wire clamps used in the SSF prototypes were used to avoid slippage in the adopted grips shown in figure 3(b). During the tests, the temperature was monitored with three different thermocouples placed inside the chamber. One measured the temperature of the hot air inlet to provide a feedback loop for the chamber controller; the other two were used to measure the temperature of the metal base of the grips, as they represent the parts with the higher thermal inertia in the chamber (as shown in figure 3(b)). When mounted, the wires were left in the chamber for one hour to ensure a complete heating up of the entire system and specimen. For the same reason, when the testing temperature was changed between the three reference temperatures (80 °C, 90 °C and 100 °C) 45 min were waited before the starting of any test.

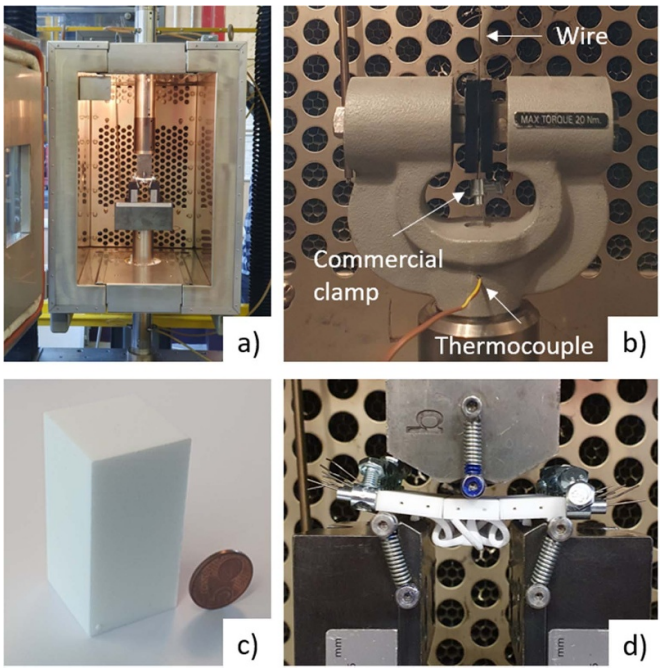

Figure 3. (a) The environmental chamber used in the high temperature tests; (b) a SMA wire specimen; (c) PA12 specimen for the compression tests; (d) bending fixture with an SSF specimen in position.

The wires' ends relative displacement was directly obtained from the one of the machine's crossheads. Considering the low registered forces (always below 0.1 kN), the machine likely underwent negligible deformation, and the stiffness of the crosshead was thus neglected. The displacement was applied with a 5 mm min^{-1} rate that is sufficiently low to avoid possible dynamical effects and to avoid influences on the SMA transformation process. Three specimens for each temperature were tested; at each temperature, two load cycles were performed. This allowed to calculate a confidence interval on the extrapolated material parameters.

Seven material parameters for each temperature were extracted from the obtained material curves to model the super-elastic behaviour on Abaqus [28]. This extraction required an extrapolation procedure shown in figure 4 and described as follows [29]. First, line p was created by linearly interpolating the upper plateau region in the chosen interval of strain ranging from 2% to 4%. This interval was selected as the one that better included the upper plateau, as no standard procedure is defined in literature. Point A^* was identified as the intersection of the line p with the unloading part of the curve. Then, line m^* was drawn as the tangent to the curve passing through point A^*. Point A was identified as the first point of the line p to be lower than 10 MPa of the whole curve. Finally, line m was drawn as the line with the same slope of line m^* passing through A. Finally, line k and line h are obtained as a linear fit of the lower plateau and the loading part of the curve, respectively.

The outlined geometrical construction allowed the identification of the *stress of start* and *stress of finish* for the

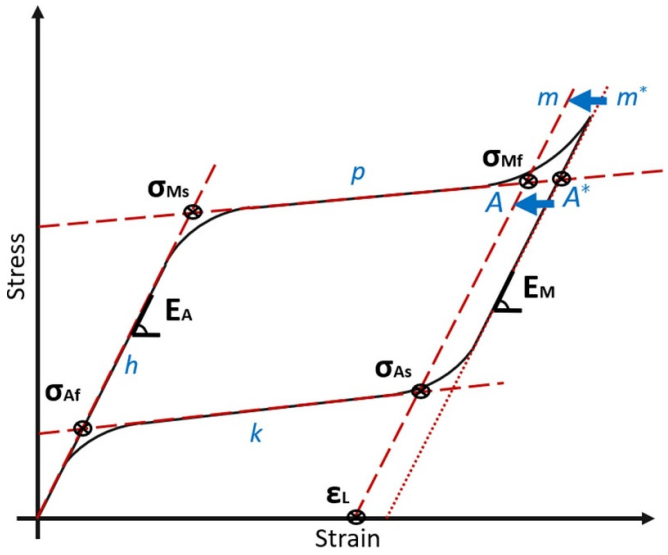

Figure 4. Superelasticity parameters extrapolation.

austenite–martensite and the martensite–austenite transformations: $\boldsymbol{\sigma}_{\mathbf{Af}}$ is the intersection of lines k and h; $\boldsymbol{\sigma}_{\mathbf{Ms}}$ is the intersection of lines p and h; $\boldsymbol{\sigma}_{\mathbf{Mf}}$ is the intersection of lines p and m; $\boldsymbol{\sigma}_{\mathbf{As}}$ is the intersection of lines k and m. The elastic modulus of martensite $\mathbf{E}_{\mathbf{M}}$ and austenite $\mathbf{E}_{\mathbf{A}}$ were calculated as the slope of the line m and h, respectively. The strain $\boldsymbol{\varepsilon}_{\mathbf{L}}$ was found as the intersection point of line m with zero stress level.

2.2.2. PA12 tests. PA12 specimens were tested under compression to characterise the material's compressive behaviour at high temperatures. Prismatic specimens of dimensions 30 × 30 × 60 mm were tested (shown in figure 3(c)). The dimensions were selected to avoid premature buckling. The displacement was applied with a rate of 5 mm min^{-1}. At first, the plates were pushed one against the other, without any specimen, to evaluate the compressive stiffness of the machine, which was later compensated for. Using the environmental chamber, the compression tests were performed at 25 °C (room temperature), 80 °C, 90 °C and 100 °C, with three specimens for each temperature to calculate the confidence bands (a total of 12 specimens were tested). A waiting time of 1 h and 30 min was established to ensure the correct temperature of the tested specimen. The end point was set to 16% of strain; this value was considered sufficiently high to describe the region of interest for the purpose of this work (elastic part). The elastic modulus of the material was calculated as prescribed in the ASTM D695 standard [30].

2.2.3. SSF validation tests. The fabric prototypes were tested in three-points bending to validate their tuneable stiffening capabilities. Figure 3(d) shows the three points bending fixture, which featured three 5 mm rollers, together with the specimen placement in testing configuration. Two thermocouples were placed to check the temperature of the specimen. One of these was positioned in the bulky metal base. The other was placed in a free hole of one of the plates of the specimen to monitor the temperature experienced by the wires inside the plates. For the high temperatures tests, the entire system (specimen, machine's grips, environmental chamber) was left to heat for 1 h and 30 min. Before increasing the test temperature, the specimens were cooled down completely before being heated up again. In this way, the stress in the wires was brought to zero before another phase transformation of the SMA wire occurred. A time of 1 h was established to let the specimen reach the target temperature. All the waiting times were established on the temperature readings from the thermocouples.

To characterise the SSF performance in the inactive configuration, the first set of tests was performed at room temperature. These tests would serve as a baseline against which the stiffness increase would be evaluated.

The bending tests were conducted applying a crosshead displacement to each of the four specimens and then removing it. The stroke applied at 80 °C was set at 3 mm for the specimens 1, 2 and 4 while at 4 mm for the specimen 3; the strokes at the other temperatures were all set to 2 mm. A preload of 10 N was applied before the test to ensure a consistent starting point for all tests. The displacement was applied with a rate of 5 mm min^{-1}.

2.3. Numerical analyses

FE simulations of the bending tests were performed to understand the mechanics of the SSFs and tune the initial spacing between the cells. The FE simulations provide information about the stress experienced by the wire, the pressure distribution between the plate and their variations during bending.

Some simplifications of the real specimen were adopted in the FE model to reduce the complexity and the computational effort. First, the connecting branches were not modelled because they do not carry load in the bending test. In addition, only one of the five rows of plates in the tested specimens was simulated, since the wires only run along one direction, and the SSFs thus behaved as several rows in parallel. The contribute of side interactions between the cell rows were neglected in this phase. Finally, two symmetry planes were identified in the simulated three-cells row and used to further reduce the model's size. The simulated portion of the fabrics is shown in figure 5(a). The final model was thus composed of three parts: a quarter of the central plate, half of the lateral plate and half of the wire. The assembly of the system is visible in figure 5(b).

Figure 5(c) highlights that the wire is initially shorter than the total length of the two plates by a length δ. This difference in length allowed to simulate the activation of the SMA wire: part of the total wire shrinkage closes the initial plates' spacing, while the rest contributes to jam the plates. The parameter δ represents this last contribution, i.e. the difference between the total shrinkage of the wire and the initial spacing of the plates. Moreover, by varying the parameter δ, it is thus possible to simulate different initial spacing of the plates. The wire's cross-section and the surface of the lateral plate opposite to the XY-plane of symmetry (right hand side of figure 5(c)) are constrained to move together. Therefore, by closing the gap δ with a z-displacement on the opposite wire's end all the

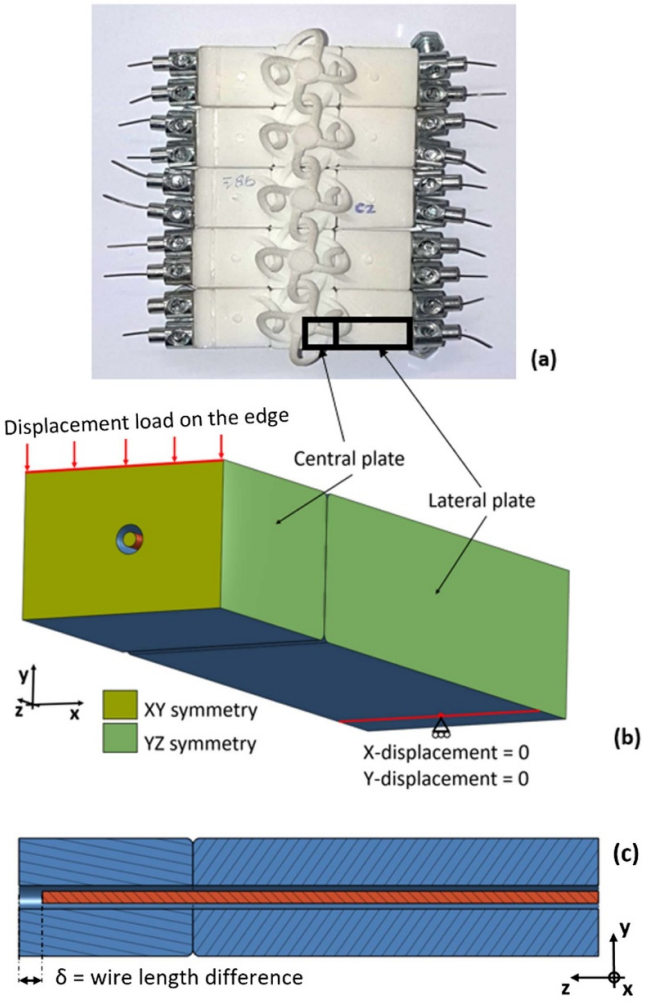

Figure 5. (a) Model simplification; (b) model with load and boundary conditions; (c) SMA wire inside the plates.

plates are put in compression by the wire. This thus simulates the activation phase of the SSF.

The super-elastic material properties of the wire were defined using the dedicated material model in Abaqus [28]. The parameters extraction is described in section 2.2, while the numerical values of these parameters are reported in table 3 in section 3.1. The PA12 material was modelled by using as input the entire stress–strain curves obtained from the compression tests, as reported in section 2.2. By using the different material parameters at different temperatures, it is possible to simulate the tests at the different temperatures.

Non-penetration contacts were modelled between the two plates and between the plates and the wire. Friction coefficients of 0.4 and 0.2 were used for the nylon–nylon contact and for the nylon–metal contacts, respectively as obtained from the literature [31–33].

The entire bending test simulation was divided into two sequential simulation steps. In the first step, the wire is stretched by a length δ to equal the plates' length, to simulate the SSF activation, as explained above. The wire thus behaves like a super-elastic spring that compresses the plates. In the second step, a vertical displacement was applied on the upper edge of the *XY* face of central plate (see figure 5(b)).

Table 2. FE simulations summary.

T (°C)	80	90	100
Spacing (mm)	0.70	0.70	0.70
	0.80	0.80	0.80
	0.90	0.90	0.90
	1.00	1.00	1.00
	1.10	1.10	1.10
	1.15	1.15	1.15
	1.20	1.20	1.20
	1.25	1.25	1.25

Symmetry boundary conditions were applied on the *XY* surfaces (yellow in figure 5(b)) and *YZ* surfaces (green in figure 5(b)) of the two plates and on the wire's cross-section (yellow in figure 5(b)). Note that the boundary condition on the wire's cross-section is applied in the second step since, initially, it does not lie on the symmetry plane. Finally, a roller kinematic constraint was applied on the red line in figure 5(b). It allows only the displacement along the *Z*-axis and the rotation around the *X* axis, to simulate the roller of the experimental bending setup.

Quadratic C3D20 elements were use for all of the three parts. The global element size was set to 0.4 mm for the plates and 0.1 mm for the wire. Refinements were applied on the contact surfaces of the plates, where an element size of 0.15 mm was considered.

For each temperature a set of simulation with different initial plates' spacings was performed. A summary of the performed simulations is provided in table 2. The upper value of the spacing was chosen to be equal to the maximum wire shrinkage upon activation: with spacings higher than 1.25 mm the plates would not be jammed by the wire. On the other hand, for spacings of 0.7 mm or lower, the stress in the wires was found to reach the super-elastic plateau during the SMA activation phase. As a result, the force applied by the wire remains constant during the fabric bending.

3. Results and discussion

3.1. Uniaxial tests of SMA and PA12 materials

In figure 6(a) shows the super-elastic curves of the SMA wires for the chosen testing temperature. They were fitted as described in section 2.2 to extrapolate the material parameters listed in table 3; confidence band with significance level $\alpha = 0.1$ are reported. As shown, all three curves present the expected super-elastic behaviour, with horizontal or close-to-horizontal upper and lower plateau that facilitated the identification of the required parameters.

The validation of the adopted material model for the SMA was also performed. To this end, simulations were perform where a single beam element was put in pure tension. The resulting stress–strain relations for the different models at different temperatures were compared with the input experimental

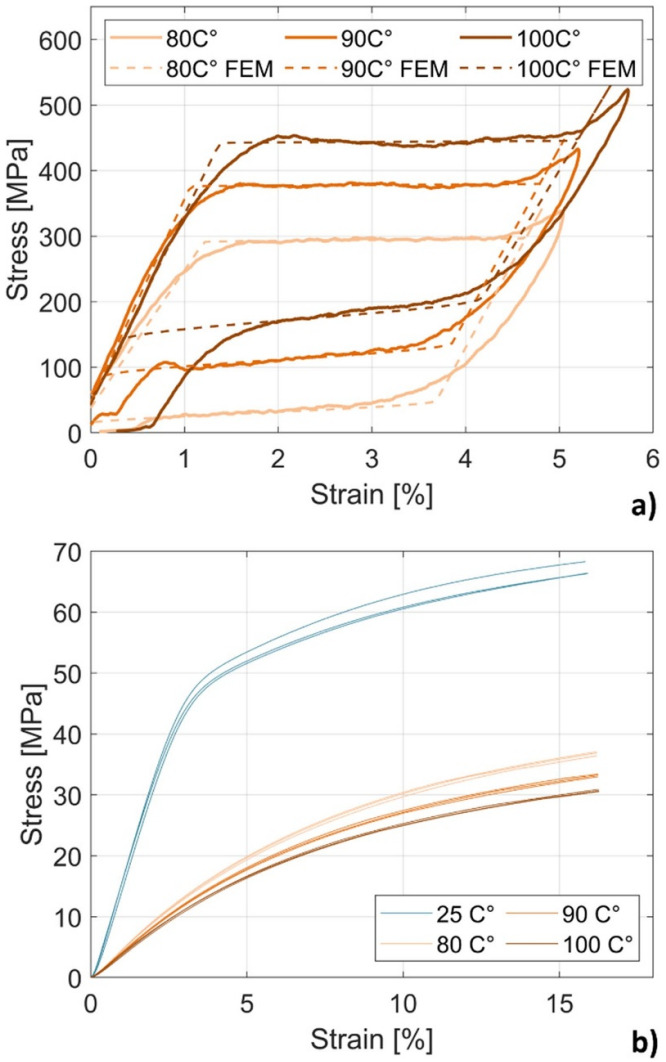

Figure 6. (a) SMA's super-elastic behaviour (experimental in continuous line and numerical in dashed line); (b) PA12 compression tests at different temperatures.

Table 3. Super-elastic parameters extracted from the experimental data at different temperature (± denotes confidence band).

T (°C)	80	90	*100*
E_A (MPa)	20 667 ± 548	28 667 ± 3838	29 733 ± 1046
E_M (MPa)	26 500 ± 822	26 167 ± 274	25 400 ± 1834
σ_{Ms} (MPa)	288 ± 8	372 ± 4	440 ± 3
σ_{Mf} (MPa)	301 ± 8	373 ± 6	464 ± 24
σ_{As} (MPa)	44 ± 11	124 ± 11	187 ± 19
σ_{Af} (MPa)	11 ± 10	74 ± 10	139 ± 3
ε_L (%)	3.7 ± 0.3	3.5 ± 0.0	3.7 ± 0.2

curves in figure 6(a). As shown, the numerical curves agree with reasonable accuracy with the experimental input, proving the validity of the adopted material models.

The compression experimental curves of the PA12 specimens are shown in figure 6(b). A significant reduction of the strength and elastic modulus with temperature is clearly visible from the plot. The material behaviour was modelled using

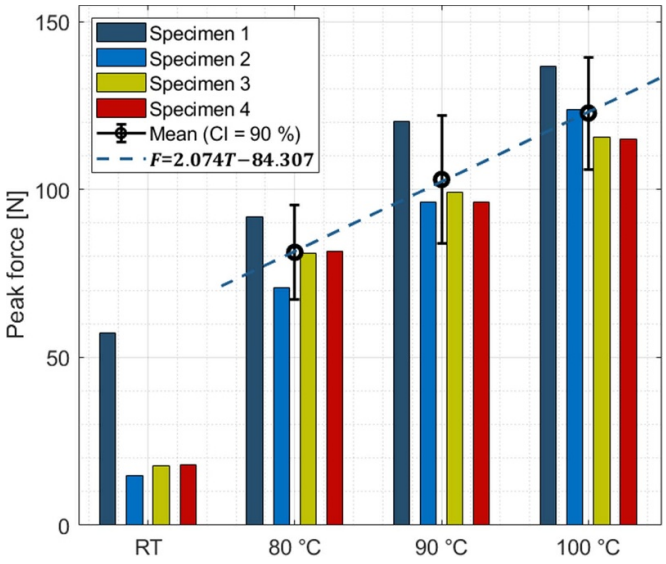

Figure 7. Effect of temperature on the measured peak load with 2 mm stroke for each specimen.

experimental data in the FEM to account for the softening due to temperature and better represent the system.

3.2. SSF test results

Figure 7 shows the values of the measured peak force in the bending tests, at different temperatures and for each specimen, as an indication of the stiffening of the SSFs. The temperature's stiffening effect is clearly shown in the histogram: the peak force increases from room to high temperature, but also among different high temperatures (80 °C, 90 °C and 100 °C). This confirms that the SSFs can potentially feature a tuneable stiffness with temperature. Even considering the different variability in the peak forces obtained among all prototypes, the trend of increasing stiffness with increasing temperature is shown to be repeatable and consistent.

The registered force at each temperature is reported in figure 8 for each of the four specimens as a function of the machine head stroke. The plots show the loading phase of the SSFs for the first 2 mm strokes. As expected, the fabric specimens in their inactive state behave similarly to a foldable object, with a near-zero initial bending stiffness. Nevertheless, a certain stiffening trend is observed, especially for specimen 1, due to the prototype starting to pull on the SMA wires' ends. However, significantly larger forces are reached in the high-temperature tests, when the SSFs are in their active configuration.

As shown, all specimens displayed different values of maximum force at different temperatures. These force differences among the same temperature can be attributed to little differences in the initial spacing between the plates. Overall, the responsive stiffness capability of the proposed SSFs is demonstrated.

In particular, specimen 1 responded with higher recorded forces than all other specimens at all temperatures. Even if the prototypes are nominally identical in geometry, manufacturing

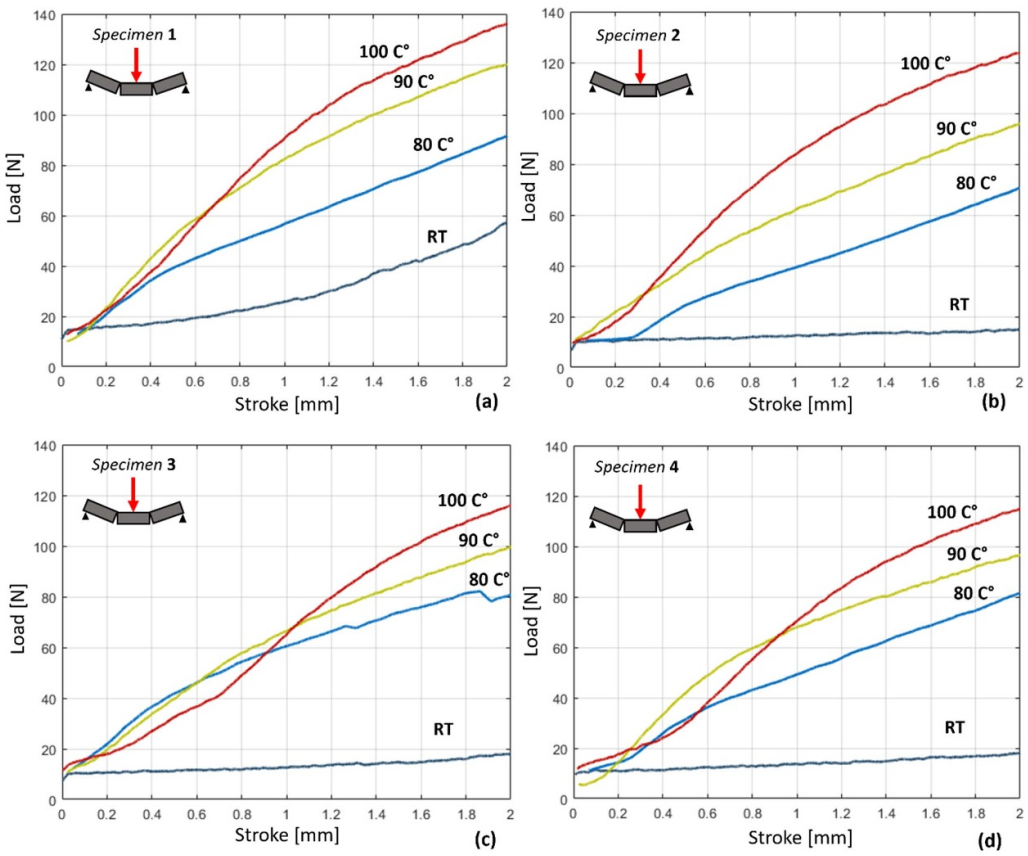

Figure 8. 2 mm stroke cycle at RT, 80 °C, 90 °C and 100 °C for specimen 1 (a), specimen 2 (b), specimen 3 (c) and specimen 4 (d).

technique and assembling procedure, their three-point bending behaviour resulted slightly different. As later discussed in section 3.3, this is likely due to the difficult assembly process that cannot guaranties a high level of precision and good tolerances, especially on the initial spacing between the cells. The experimental SSF behaviour was anyway in line with the FEM simulation results as shown in figure 9 of the next section.

The stiffness percentage variation between the different temperature in the active state (80 °C, 90 °C, 100 °C) are reported in table 4, showing an average of 27% and 20% stiffness increase from 80 °C to 90 °C, and from 90 °C to 100 °C, respectively. The stiffness increase from room temperature could not be quantified accurately, as in the inactive state, the prototypes showed a near-zero stiffness: the measured forces were considered too low to be attributed to the prototype stiffness, and rather result from frictions or other phenomena.

Note that the reported stiffness increases for the SSFs are obtained at high temperatures, where the PA12 shows about 80% stiffness reduction (see figure 6(b)). The effectiveness of the stiffening effect is thus able to overcome the softening of the polymer.

3.3. Numerical results and comparison with experiments

From the developed FE model of the bending test, a set of simulations with different plates' spacings was performed for each temperature. The results are summarized in figure 9 where the force curves for different spacings are plotted together with the experimental data. The chosen values of spacings range from 1.25 mm to 0.7 mm. The light blue area represents the working region of the SSF in the force-stroke chart. By changing the spacing value, a different bending force inside that region can be achieved and so a different fabric stiffness. The light red and light yellow areas represent unreachable regions by the SSF force. They are delimited by the limit spacing values of 0.7 mm and 1.25 mm described in section 2.3.

As shown in figure 9, the experimental data are inside the feasibility region and the value of the real spacing of the specimens can be estimated to be in the interval of 0.8 mm and 1.2 mm. The variability of the experimental results is likely due to the high complexity of the real system that includes up to 48 parts (plates, wires, clamps, rollers) with all the associated contacts and geometrical imperfections. It is also likely that initial imperfections in the relative position of the plates likely cause different responses of the SSF. Nevertheless, the tested prototypes showed a relative consistent behaviour given the similar initial spacing and assembling techniques. Indeed, the FE analyses showed a far wider possible operating region than that observed experimentally. In light of this operative region, the differences between the experimental cases appear less significant.

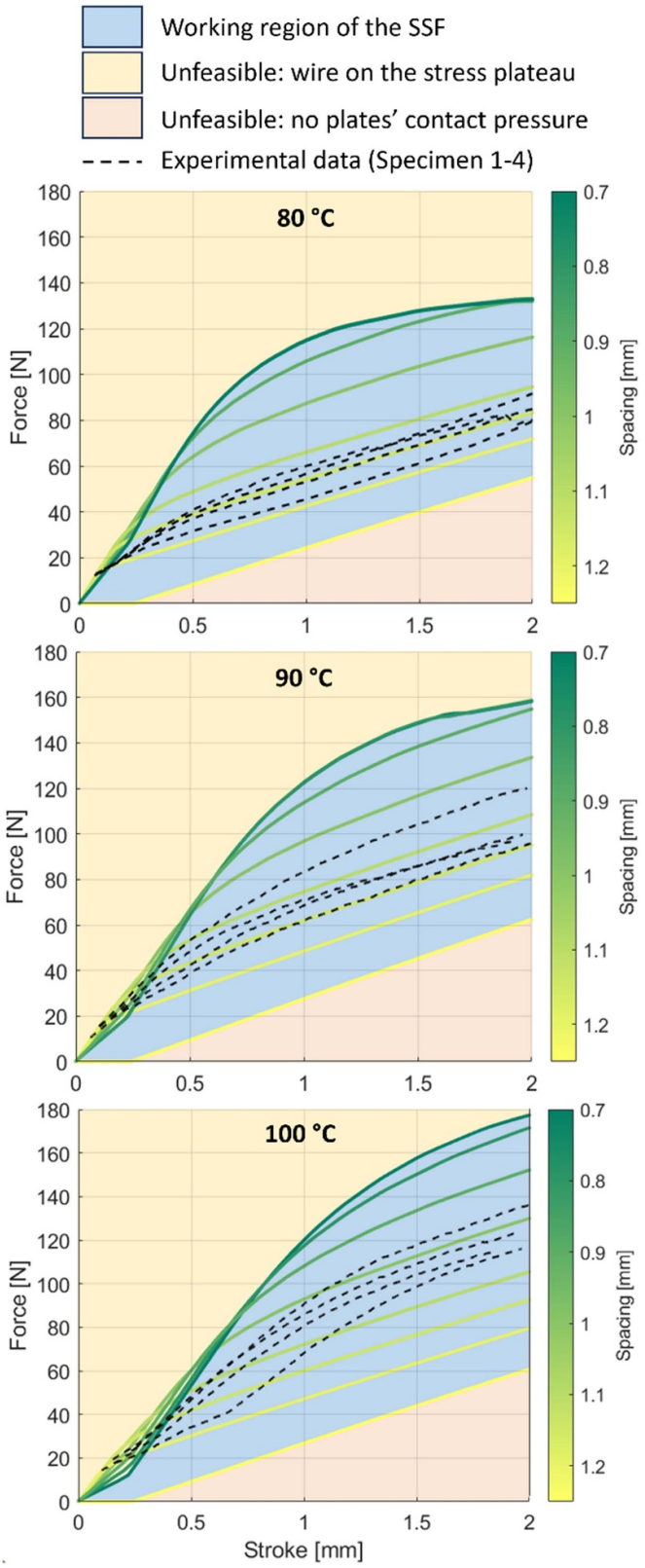

Figure 9. FE results and comparison with experimental data.

Moreover, the analyses showed how sensitive the overall performance of the SSFs are to the initial spacing. Such sensitivity, in addition to the loose control on the spacing of the adopted assembling procedure, further suggest that this is the main cause for the experimental variability between the specimens. In the future, relying on an industrial-grade precision (not possible on a prototypical production), the SSF stiffness in the active configuration can thus be accurately imposed for a specific application.

Table 4. Percentage increments of the SSF stiffness under bending test.

	$80\,^{\circ}C \rightarrow 90\,^{\circ}C$	$90\,^{\circ}C \rightarrow 100\,^{\circ}C$
Specimen 1	+31%	+14%
Specimen 2	+36%	+29%
Specimen 3	+22%	+17%
Specimen 4	+18%	+19%
Average	+27%	+20%

3.4. Innovation and potential applications

The present work aimed to present the SSF working concept and prove its functionality and feasibility. Nevertheless, SSF's specific properties makes it possible to identify some potential fields of application. The space industry, for example, could exploit the SSFs' variable stiffness for deployable structures [34]. SSFs can be more easily stored in their inactive configuration, thanks to the low stiffness. Once necessary (for example once in orbit), an SSF-based structure can be unfolded into its final operative shape. SSF's temperature sensitivity would also make them suitable for deployable heat shields: this would require the use of a ceramic mail or simply ceramic tiles to be bonded on a metallic mail.

Wang *et al* highlighted how fabrics-like structure can adhere to complex surfaces, including the human body [10]. Similarly to their proposed structured fabrics, SSFs can thus also be employed for wearable exoskeletons: in their inactive state, they can be worn and adjusted to fit the wearer, in their active configuration they can support heavy activities like weight carrying. Wang *et al* also proposed the use of double stiffness fabrics in reconfigurable architecture [10].

Note that the above are examples of potential applications, but more are possible. As mentioned, figure 9 shows a vast possible operating region by only adjusting the initial spacing between the plates. This region can be further expanded by considering different materials for the mail or the shape-memory element. In particular, for the former, materials less susceptible to high-temperature softening (like metals) can lead to drastically higher stiffnesses increases; for the latter, different materials would also allow an additional control on the activation temperature ranges, since SMAs with different transformation temperatures can be employed. However, the adoption of different materials (for both the chainmail and the SMA) or different geometrical configuration may lead to different stiffness variations. For this reason, the present work should be intended as a validation of an innovative concept, while new SSFs formulation should be characterised each time (as is the case for new materials and meta-materials).

The experimental tests (see figure 7) also highlight the dependence of the stiffness on the operational temperature of

the SSF. In this work, heating was provided via an environmental chamber, but electric heating of the SMA wire via Joule effect could also be another possibility. Such an active heating could be implemented a closed-loop control on the wire temperature, which can thus be tightly controlled resulting in a specific stiffness selection.

Finally, the variable stiffness can be a crucial property in application were the dampening of the vibrations is of central importance or where the mechanical properties of the structure have to adapted to the environment. Overall, geometry, assembling parameters, materials and activation modes are all possible features that can specialise the SSF concept to a specific application.

4. Conclusions

A new concept of smart fabric, namely SSFs, are here presented. SSFs are composed of 3D printed chainmail assembled with SMA wires. The cells of the chainmail are designed to allow the initial interconnection, to host the SMA wires and to provide a certain plate-like behaviour in the active configuration. Moreover, their ability of being 3D printed already assembled allow for a fast and easy manufacturing phase. The SMA wires make the whole system responsive to the external temperature. Through bending tests at different temperatures, it was shown how the proposed SSFs are capable of:

- A near-zero bending stiffness below the SMA activation temperature.
- A significant stiffness increase above the SMA activation temperature with respect to the room temperature.
- A temperature-dependent stiffness for temperatures above the SMA activation temperature, with temperature increases ranging from 1.4% to 3.6% per degree.

To the best of our knowledge, the proposed SSFs are the first devices capable of achieving the results outlined above without the need of energy intensive or bulky external devices, like vacuum pumps or magnetic devices.

Numerical analyses were also conducted for a deeper study of the SSFs' behaviour. In particular, it was shown the key role of the initial inter-plates spacing in affecting the SSF response. The spacing is responsible of the overall final stiffness of the SSF in the active configuration and the stress state in the SMA wires, thus its precise tuning is of paramount importance for reaching a target SSF stiffness.

The SSF concept proposed in this work was validated with polymeric chainmail and commercially available nitinol wires. However, the concept itself is not dependent on the material adopted, and therefore different combinations can potentially be investigated. Varying the chainmail material can lead to different SSFs response: a metallic chainmail, for example, can lead to higher stiffnesses to be achieved but also to a faster activation, thanks to the higher thermal conductivity. Moreover, the choice of different SMA would imply different activation temperatures, thus changing the SSF active and inactive temperatures and expanding the range of applications for such innovative structures. Other possible variations to be investigated in future studies include different cells designs and shape, chainmail featuring larger number of cells, a different wire distribution and an active control on the SSF via electric heating.

Overall, this work sets the basis for an innovative concept of smart structures, whose stiffness can be tuned based on their operating temperature. The near-zero bending stiffness in the inactive configuration is also an interesting property, since it allows to design foldable SSFs that can be than deployed in a high-temperature environment. Potential applications of such structures range from space applications, for which foldable/deployable structures are of high interest, robotics, where energy efficient actuation is often desirable, and more.

Data availability statement

All data that support the findings of this study are included within the article (and any supplementary files).

ORCID iDs

Marco Rossoni https://orcid.org/0000-0003-2714-9043
Luca Michele Martulli https://orcid.org/0000-0002-1754-9054

References

[1] Zadpoor A A 2016 Mechanical meta-materials *Mater. Horiz.* **3** 371–81
[2] Wang K, Chang Y H, Chen Y W, Zhang C and Wang B 2015 Designable dual-material auxetic metamaterials using three-dimensional printing *Mater. Des.* **67** 159–64
[3] Barchiesi E, Spagnuolo M and Placidi L 2019 Mechanical metamaterials: a state of the art *Math. Mech. Solids* **24** 212–34
[4] Bloomfield M and Borstrock S 2018 Modeclix. The additively manufactured adaptable textile *Mater. Today Commun.* **16** 212–6
[5] Spahiu T, Canaj E and Shehi E 2020 3D printing for clothing production *J. Eng. Fiber Fabr.* **15** 1–8
[6] Melnikova R, Ehrmann A and Finsterbusch K 2014 3D printing of textile-based structures by fused deposition modelling (FDM) with different polymer materials *IOP Conf. Ser.: Mater. Sci. Eng.* **62** 012018
[7] Partsch L, Vassiliadis S and Papageorgas P 2015 3D printed textile fabrics structures *5th Int. Istanbul Textile Congress 2015: Innovative Technologies Inspire to Innovate* pp 3–10
[8] Ploszajski A R, Jackson R, Ransley M and Miodownik M 2019 4D printing of magnetically functionalized chainmail for exoskeletal biomedical applications *MRS Adv.* **357** 1–8
[9] Chu JJennifer 2019 Engineers 3-D print flexible mesh for ankle and knee braces, MIT engineers 3-D-print stretchy mesh, with customized patterns designed to be flexible yet strong, for use in ankle and knee braces (available at: http://news.mit.edu/2019/3-d-print-mesh-ankle-knee-braces-0619) (Accessed 03 June 2024)
[10] Wang Y, Li L, Hofmann D, Andrade J E and Daraio C 2021 Structured fabrics with tunable mechanical properties *Nature* **596** 238–43
[11] Ransley M, Smitham P and Miodownik M 2017 Active chainmail fabrics for soft robotic applications *Smart Mater. Struct.* **26** 08LT02

[12] Engel J and Liu C 2007 Creation of a metallic micromachined chain mail fabric *J. Micromech. Microeng.* **17** 551–6
[13] Halbrecht A, Kinsbursky M, Poranne R and Sterman Y 2023 3D printed spacer fabrics *Addit. Manuf.* **65** 103436
[14] Khalid M Y, Arif Z U, Ahmed W, Umer R, Zolfagharian A and Bodaghi M 2022 4D printing: technological developments in robotics applications *Sens. Actuators* A **343** 113670
[15] Shukla U and Garg K 2023 Journey of smart material from composite to shape memory alloy (SMA), characterization and their applications-a review *Smart Mater. Med.* **4** 227–42
[16] Yuen M, Cherian A, Case J C, Seipel J and Kramer R K 2014 Conformable actuation and sensing with robotic fabric *IEEE/RSJ Int. Conf. on Intelligent Robots and Systems* (IEEE) pp 580–6
[17] Kamila S 2013 Introduction, classification and applications of smart materials: an overview *Am. J. Appl. Sci.* **10** 876–80
[18] Mohd Jani J, Leary M, Subic A and Gibson M A 2014 A review of shape memory alloy research, applications and opportunities *Mater. Des.* **56** 1078–113
[19] Shaw J A, Churchill C B and Iadicola M A 2008 Tips and tricks for characterizing shape memory alloy wire: part 1-differential scanning calorimetry and basic phenomena *Exp. Tech.* **32** 55–62
[20] Ahmed F, Waqas M, Shaikh B, Khan U, Soomro A M, Kumar S, Ashraf H, Memon F H and Choi K H 2022 Multi-material bio-inspired soft octopus robot for underwater synchronous swimming *J. Bionic Eng.* **19** 1229–41
[21] Tadesse Y, Hong D and Priya S 2011 Twelve degree of freedom baby humanoid head using shape memory alloy actuators *J. Mech. Robot.* **3** 1–18
[22] Chaurasiya K L, Harsha A S, Sinha Y and Bhattacharya B 2022 Design and development of non-magnetic hierarchical actuator powered by shape memory alloy based bipennate muscle *Sci. Rep.* **12** 1–15
[23] Yang X, Chen Y, Chen T, Li J and Wang Y 2024 Active fabrics with controllable stiffness for robotic assistive interfaces *Adv. Mater.* **36** 2404502
[24] Sun Y, Li C, Xu Z, Cao Y, Sheng H, Wang Z L and Cao L N Y 2023 Conformable multifunctional space fabric by metal 3D printing for collision hazard protection and self-powered monitoring *ACS Appl. Mater. Interfaces* **15** 5772637
[25] SAES group 2020 SmartFlex data-sheet vol 5 pp 248–53
[26] Landau E 2017 *'Space Fabric' Links Fashion and Engineering* (available at: www.jpl.nasa.gov/news/space-fabric-links-fashion-and-engineering/) (Accessed 03 June 2024)
[27] EOS EOS polyamide 12 powders for 3D printing (available at: www.eos.info/en-us/polymer-solutions/polymer-materials/multipurpose#pa-2200-balance) (Accessed 03 June 2024)
[28] Dassault Systèmes 2021 Abaqus 2021 User's Manual - Superelasticity material behaviour (Accessed 03 June 2024)
[29] Roberto-Pereira F F, Campbell J E, Dean J and Clyne T W 2019 Extraction of superelasticity parameter values from instrumented indentation via iterative FEM modelling *Mech. Mater.* **134** 143–52
[30] American Society for Testing and Materials International 2002 Standard test method for compressive properties of rigid plastics D695 *ASTM Int.* **08** 1–7
[31] Aldahash S 2021 Friction and wear properties of oriented polyamide 12 objects manufactured by SLS technology *J. Eng. Appl. Sci.* **8** 28
[32] Yu G, Ma J, Li J, Wu J, Yu J and Wang X 2022 Mechanical and tribological properties of 3D printed polyamide 12 and SiC/PA12 composite by selective laser sintering *Polymers* **14** 2167
[33] Kundera C and Kozior T 2018 Mechanical properties of models prepared by SLS technology *AIP Conf. Proc.* **2017** 020012
[34] Wang B, Zhu J, Zhong S, Liang W and Guan C 2024 Space deployable mechanics: a review of structures and smart driving *Mater. Des.* **237** 112557